

Article

Enhanced Performance of nZVI/MXene@CNTs for Rapid As(III) Removal from Aqueous Solutions

Shihai Li ¹, Siyuan Luo ^{1,2}, Si Wan ^{3,4,*}, Ping Wang ¹, Gang Zhou ¹, Wenming Wang ⁵ and Runhua Chen ^{1,*}

¹ College of Environmental Science and Engineering, Central South University of Forestry and Technology, Changsha 410007, China

² China Gezhouba Group Water Operation Co., Ltd., Wuhan 430030, China

³ Hunan Research Institute for Nonferrous Metals Co., Ltd., Changsha 410100, China

⁴ Faculty of Environmental Science and Engineering, Kunming University of Science and Technology, Kunming 650500, China

⁵ Hunan Pilot Yanghu Reclaimed Water Co., Ltd., Changsha 410006, China

* Correspondence: chen12@csuft.edu.cn (R.C.); wanlion301@163.com (S.W.); Tel.: +86-18175191572 (S.W.); Fax: +86-731-85239126 (S.W.)

Highlights:

- nZVI/MXene@CNTs with a three-dimensional intercalation structure was successfully synthesized.
- nZVI/MXene@CNTs exhibited a high adsorption and catalytic oxidation capacity for As(III).
- nZVI/MXene@CNTs showed good anti-interference ability.
- nZVI/MXene@CNTs possessed excellent recyclability and reusability.

Abstract: Transition metal compounds demonstrated good performance in the removal of environmentally harmful contaminants, such as arsenic, while the aggregation propensity and poor chemical stability should be noticed. In this study, the nZVI/MXene@CNTs was adequately prepared by liquid reduction precipitation method for adsorption and oxidation of As(III) from the aqueous solution. The results of batch removal experiments showed that the maximum removal capacity of the nZVI/MXene@CNTs for As(III) was 443.32 mg/g with the pH = 3.0 at 25 °C. The effects of initial pH, dosage of materials and ionic strength on As(III) removal were explored. According to the various characterization analyses, the most plausible mechanisms of As(III) removal were the surface complexation, solid phase precipitation and the catalytic oxidation by the •OH. Furthermore, the nZVI/MXene@CNTs could be readily activated and reused via leaching with 0.1 M NaOH solution, due to the three-dimensional mesh intercalation structure. Therefore, it is a potential nanocomplex for removing and recovering As(III) from water with excellent capacity and environmental friendliness.

Keywords: MXene; nZVI; intercalation structure; As(III); reusability; water treatment



Citation: Li, S.; Luo, S.; Wan, S.; Wang, P.; Zhou, G.; Wang, W.; Chen, R. Enhanced Performance of nZVI/MXene@CNTs for Rapid As(III) Removal from Aqueous Solutions. *Appl. Sci.* **2022**, *12*, 8206. <https://doi.org/10.3390/app12168206>

Academic Editor: Franz Jirsa

Received: 19 June 2022

Accepted: 12 August 2022

Published: 17 August 2022

Publisher's Note: MDPI stays neutral with regard to jurisdictional claims in published maps and institutional affiliations.



Copyright: © 2022 by the authors. Licensee MDPI, Basel, Switzerland. This article is an open access article distributed under the terms and conditions of the Creative Commons Attribution (CC BY) license (<https://creativecommons.org/licenses/by/4.0/>).

1. Introduction

Arsenic (As(III)) poses a serious ecological concern due to its toxicity and prevalence in the environment [1,2]. The metalloid properties of arsenic mean that when talking about the environmental problems that it causes, heavy metal pollution is commonly brought up. Arsenic-containing wastewater is widely sourced from industrial activities, such as electroplating, chemical, mining and smelting with poisonous, migratory, and carcinogenic, causing substantial environmental issues and even considerable human health risk [3]. To prevent the negative effects of As(III) on the environment, the World Health Organization set a maximum of 10 µg/L for arsenic in the international drinking-water standards [4]. Thus, purifying arsenic-containing wastewater is one of the most critical environmental issues that needs immediate attention.

There are various forms of As(III) in industrial wastewater, including AsO_3^{3-} , AsO_4^{5-} and the crystal shape of arsenite [5,6]. Because of being more toxic than its oxidized form

in wastewater, As(III) has drawn greater attention [7]. The conventional methods were employed for the removal of As(III) from industrial wastewater, including coagulation precipitation [8], electro flocculation [9], ion exchange [10], membrane separation [11], biological methods [12] and adsorption [13]. Adsorption technology, due to its wide adaptability, environmental friendliness and economic characteristics, is regarded as a simple and effective strategy [14,15]. Consequently, attention has shifted to the innovative synthesis and application of adsorbent materials [16,17]. Ghorbanzadeh [18] et al. investigated kaolinite, montmorillonite and nontronites for As(III) wastewater treatment, and discovered that nontronite with a greater iron concentration (37.63%) had the highest As(III) adsorption capability (0.68 mg/g), compared to montmorillonite (0.26 mg/g) and kaolinite (0.24 mg/g). Chammui [19] et al. developed a Leonardite activated-carbon as an adsorbent for the removal of As(III) with an adsorption capacity of 4.5 mg/g, which realized the resource utilization of mine waste. Niazi [20] et al. produced pyrolyzed oakwood BC with 3.16 mg/g As(III) removal capacity and revealed that a large BC surface area (475 m²/g) and pore volume (0.2 cm³/g) could be formed after high temperatures of 500 °C. Although many natural materials were used for the adsorption of heavy metals due to their low cost, easy access and quick adsorption, the poor removal capability limited their widespread application [21].

Recently, nanotechnology has attracted interest for the potential to address various environmental challenges by manipulating the particle size and surface modifiers [22,23]. Many of the nanomaterials have been synthesized effectively for the purification of heavy metal wastewater, for instance, carbon nanomaterials [24], nanoscale metal-organic frameworks and their derivatives [25] and transition metal composite nanomaterial, such as iron nanoparticles [26], transition metal oxides [27] (e.g., Fe₃O₄, Ag₂O) and transition metal nanocomplex [28,29] (e.g., Co₃O₄/GO, MnO₂/Fe₂O₃@AC). Kanel [30] et al. reported that nanoscale zero-valent iron (nZVI) for As(III) adsorption quickly saturated within minutes, with a maximum adsorption capacity of 3.5 mg/g. Zhang [31] et al. synthesized bimetallic oxide magnetic nanoparticles (MnFe₂O₄ and CoFe₂O₄) for the purification of low-concentration arsenic solutions, demonstrating that MnFe₂O₄ and CoFe₂O₄ had maximum As(III) adsorption capacities of 94.00 mg/g and 100 mg/g, respectively, and the nanoparticles could be reused well by desorption. Wei [32] et al. prepared magnetic Fe–Cu/TiO₂ nanoparticles for the treatment of As(III)-containing industrial wastewater, and revealed an As(III) removal capacity of around 17.5 mg/g, and more interestingly As(III) was completely oxidized on the adsorbent. Zhang [33] et al. synthesized Al₂O₃-pillared layered MnO₂(p-MnO₂) for the adsorption of Pb(II), Cu(II) and Cd(II) in aqueous solutions, revealing that the BET surface area increased to 166.3 m²/g and the substrate spacing expanded to 0.85 nm, which showed a greater heavy-metal ion adsorption capability than MnO₂. The transition metal nanomaterials have great advantages for their controllable particle size, large surface effect, and strong adsorption capabilities to be used widely for the removal of heavy metal ions from water [34–37]. However, some of the features, such as agglomeration propensity and poor chemical stability should be noticed in certain specific areas [4,38].

In the past five years, MXene, a novel family of 2D intercalation materials, has become a research hotspot and received extensive attention. It is generally expressed as M_{n+1}AX_nT_x, formed from the layered and machinable M_{n+1}AX_n phases, where n = 1, 2, 3, M is an early transition metal; X is C or N; A is an element C or B of the periodic table, and T_x is the surface terminal group [39]. The novel materials possessed specific physicochemical properties, such as high surface areas, unique hydrophilicity, abundant surface functional groups and excellent adsorption capacity, and Ti₃C₂T_x MXene was one of the most explored composites [40]. Kim [41] et al. explored the removal of some pharmaceuticals compounds by Ti₃C₂T_x MXene and revealed the selective adsorption capacity 58.7 mg/g for cationic amitriptyline (AMT), with great reusability after sonication. Jun [42] et al. reported that Ti₃C₂T_x MXene possessed excellent selective adsorption capacity (148 mg/g) of Cs⁺ from model low-level radioactivity, achieving rapid purification and substantial reuse. Apart from their outstanding adsorption capacity, Ti₃C₂T_x MXene also has potential for

applications in catalytic oxidation [43], electrochemistry [44], photocatalysis [45] and super-sensors [46]. Therefore, it is extremely deserving of further study.

In this study, a novel three-dimensional mesh intercalation and multifunctional magnetic nanofibers hybrid (nZVI/MXene@CNTs) was prepared for As(III) wastewater treatment. A variety of the characterizations was carried out to understand the possible mechanism of the synthesis of nZVI/MXene@CNTs. It was revealed that the material possessed enhanced adsorption performance, chemical stability and catalytic capabilities. The batch adsorption experiments were utilized to evaluate the capacity of nZVI/MXene@CNTs for As(III) removal and discussed the potential effects of pH, interfering ions and other conditions. The probable adsorption mechanism and catalytic oxidation process of As(III) on nZVI/MXene@CNTs were also investigated.

2. Materials and Methods

2.1. Materials

The titanium aluminum carbide (Ti_3AlC_2) was purchased from 11 Technology Co., Ltd. in Jilin, China. The multi-walled carbon nanotubes (MWCNTs) were purchased from Suzhou CarbonFocus Graphene Technology Co., The nitric acid (HNO_3), sulfuric acid (H_2SO_4), hydrochloric acid (HCl) and sodium hydroxide (NaOH) were obtained from Tianjin Hengxing Chemical Reagent Manufacturing Co., Ltd. (Tianjin, China). The lithium fluoride (LiF), anhydrous ethanol ($\text{C}_2\text{H}_5\text{OH}$), thiourea ($\text{CH}_4\text{N}_2\text{S}$), ascorbic acid ($\text{C}_6\text{H}_8\text{O}_6$), ferrous sulphate ($\text{FeSO}_4 \cdot 7\text{H}_2\text{O}$), calcium nitrate ($\text{Ca}(\text{NO}_3)_2$), magnesium nitrate ($\text{Mg}(\text{NO}_3)_2$), sodium chloride (NaCl) and sodium sulfate (Na_2SO_4) were purchased from Sinopharm Group Chemical Reagent Co., Ltd. (Hong Kong, China). The sodium borohydride (NaBH_4), potassium borohydride (KBH_4) and sodium arsenite (NaAsO_2) were purchased from Xilong Science Co., Ltd. (Guangdong, China). All of the chemicals used were analytically pure and the water used in the experiments was ultrapure.

2.2. Synthesis of nZVI/MXene@CNTs

2.2.1. Preparation of Functionalized CNTs

A total of 2 g multi-walled carbon nanotubes (MWCNTs) was added to 80 mL of a 1:3 combination of HNO_3 and H_2SO_4 and stirred for 2 h at 80 °C. The suspension was extracted and washed with water many times until the filtrate was neutral, then dried in a vacuum drying oven at 60 °C for more than 12 h to a constant weight to get functionalized CNTs after cooling at ambient temperature and diluted several times with deionized water.

2.2.2. Synthesis of nZVI/MXene@CNTs

The Ti_3C_2 MXene dispersion followed a prior report by our research group [47]. In a mild aqueous environment, the nZVI/MXene@CNTs nanocomplex was produced using a simple self-assembly approach. Specifically, to obtain a homogeneous suspension, 0.2 g functionalized CNTs was combined with 30 mL deionized water and fully sonicated with the pre-prepared MXene dispersion. The above CNTs and MXene dispersion was added to a 5.0 g/L $\text{FeSO}_4 \cdot 7\text{H}_2\text{O}$ solution, agitated constantly to mix thoroughly, and N_2 was filtered through to remove the residual dissolved oxygen. Then, under N_2 and constant stirring, a freshly produced NaBH_4 solution with the 5.0 g/L concentration was dropped into the mixed liquid dropwise at the rate of 3.2 mL/min. Finally, the precipitates were freeze-dried in a vacuum to obtain nZVI/MXene@CNTs nanocomplex after being washed several times with water/ethanol.

2.3. Characterization

The Fourier-Transform infrared spectroscopy (FTIR; Thermo Scientific Nicolet iS5, Waltham, MA, USA) was used to analyze the chemical bonds and functional groups of functionalized CNTs, Ti_3C_2 MXene and nZVI/MXene@CNTs. The scanning electron microscopy (SEM; ZEISS Sigma 300, Roedermark, Germany) equipped with an energy dispersive X-ray spectrometer (EDS) was employed to observe the morphology and structure of several

materials. The chemical state, elemental content and molecular structure of the materials were determined applying X-ray photoelectron spectroscopy (XPS; Thermo Scientific K-Alpha) based on peak location and peak shape. The vibrating sample magnetometry (VSM; LakeShore7404) was employed to evaluate the magnetic characteristics of the samples.

2.4. Batch Removal Experiments

The As(III) removal capacity of nZVI/MXene@CNTs was investigated by batch experiments. In a 150 mL conical flask, 50 mL of different concentrations of As(III) aqueous solution were mixed with 0.4 g/L nZVI/MXene@CNTs and put on a constant temperature shaker running at 150 rpm. The effect of different factors, such as the pH and dosage of materials on the removal of As(III) by nZVI/MXene@CNTs, was investigated and the initial pH value was controlled, using 0.1 M HCl/NaOH diluent. The influence of the interfering ions on the removal ability of nZVI/MXene@CNTs was investigated by employing aqueous As(III) solutions, containing 0.01 mol/L Mg^{2+} , Ca^{2+} , Cl^{-} and SO_4^{2-} . The leaching experiment with 0.1 M NaOH solution was used to test the regeneration and recoverable function of nZVI/MXene@CNTs. The thermodynamics, kinetics and isotherms were also studied. The isotherm data were evaluated by Langmuir and Freundlich isotherm models. To fit the adsorption data, pseudo-first-order and pseudo-second-order kinetic models were employed. The residual As(III) and As(V) concentrations after filtering were measured using inductively coupled plasma mass spectrometry (ICP-MS; PerkinElmer NexION 300X, Waltham, MA, USA). The adsorption amount q_e was calculated (Equation (1)). The adsorption kinetics, isotherms and thermodynamic experiments and calculations are available in the Supplementary Materials. All of the removal experiments were repeated three times, with the average results used to assess the performance:

$$q_e = \frac{V(C_0 - C_e)}{m} \quad (1)$$

where, q_e is the adsorption capacity, mg/g; V is the volume of solution, L; C_0 is the initial concentration of As(III), mg/L; C_e is the residual concentration of As(III), mg/L; m is the adsorbent dosage, g.

3. Results and Discussion

3.1. Synthesis and Characterization of nZVI/MXene@CNTs

The three-dimensional mesh interlayered nZVI/MXene@CNTs nanomaterials were self-assembled in the given aqueous solution. As shown in Figure 1, the synthesis schematic design of nZVI/MXene@CNTs was depicted. Briefly, the functionalized CNTs and $Ti_3C_2T_x$ -MXene nanosheet dispersions were obtained by acid drenching the CNTs and etching the graphite phase MAX (Ti_3AlC_2), respectively. Then, the functionalized CNTs and MXene nanosheet mixture were distributed in the prepared ferrous-sulfate solution, while stirring constantly under N_2 protection. Due to the high surface energy and numerous hydrophilic groups, Fe(II) could be evenly disseminated on the surface of the CNTs and MXene. It would be generated by the sequential assembly of MXene and CNTs and the ordered placement of Fe(II) on their surfaces by water shear and zeta potential difference, producing a three-dimensional interconnected interlayer structure of Fe(II)/MXene@CNTs. Fe(II) was reduced to nZVI and deposited in the layer gaps and interstitial spaces of MXene and MXene@CNTs by the addition of a dilute reducing agent ($NaBH_4$). In this way, a nanomaterial (nZVI/MXene@CNTs), with three-dimensional interlayer structure and excellent adsorption and catalytic properties, was prepared. Additionally, this approach allowed for the simultaneous self-assembly of three-dimensional interlayer nanostructures with a variety of functional groups cross-linked for catalytic or interfacial activities, exhibiting the characteristics of simplicity, efficacy and environmental friendliness.

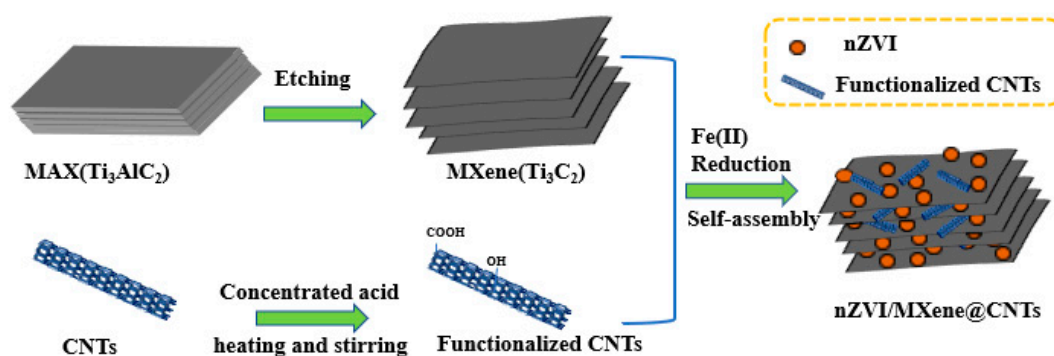


Figure 1. Schematic illustration of the self-assembly synthesis of nZVI/MXene@CNTs.

The microscopic morphology and elemental composition of the CNTs, functionalized CNTs, MXene and nZVI/MXene@CNTs were observed by SEM and EDS-mapping (Figure 2). As shown in Figure 2a, there were numerous impurities, such as amorphous carbon and agglomerates, on the original CNTs surface. However, following acidification, the surface of the CNTs became rough, showing a considerable reduction in length, diameter and impurity (Figure 2b). The prepared MXene showed a two-dimensional stack of lamellae (Figure 2c). With the addition of the nZVI and functionalized CNTs, a cross-linked and interlaced three-dimensional intercalation structure was produced, and many nZVI catalytic units were evenly coated on the surface or embedded within (Figure 2d). A considerable number of C, O, Ti and Fe elements were visible in the EDS-mapping energy spectrum (Figure 2e–h), and each element was evenly distributed on the material surface. The original morphology of nZVI/MXene@CNTs was retained after repeated ultrasonic treatment, demonstrating good stability.

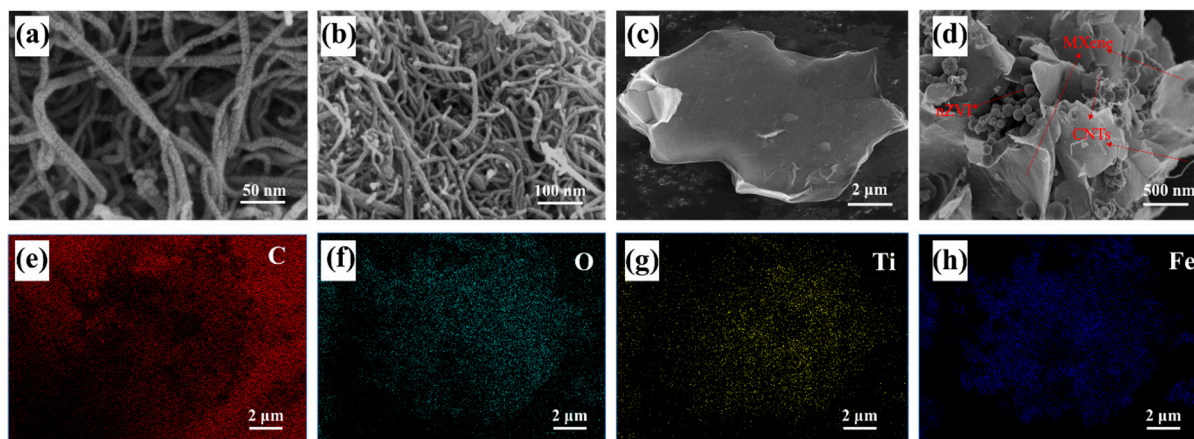


Figure 2. SEM images of (a) CNTs; (b) functionalized CNTs; (c) $\text{Ti}_3\text{C}_2\text{T}_x$ MXene; (d) nZVI/MXene@CNTs, and its EDS-mapping element images of (e) C; (f) O; (g) Ti; (h) Fe.

The functional groups of the MXene, functionalized CNTs and nZVI/MXene@CNTs nanohybrid were identified via Fourier-Transform infrared spectroscopy (FTIR) (Figure 3a). It was obvious that the number of groups on the surface of MXene was limited. In addition, the peaks at 3429 and 1325 cm^{-1} should be attributed to C-OH stretching, whereas at 2920 and 1625 cm^{-1} the peaks should be assigned to $-\text{CH}_3$ symmetric bending and C=O stretching of the carboxyl group, respectively [48]. Significantly, the new peak at 556 cm^{-1} corresponded to the Fe-O stretching vibration, indicating that the element of Fe was effectively deposited onto the surface [49]. The surface of the successfully synthesized nZVI/MXene@CNTs contained a specific quantity of iron and abundant oxygen-containing groups, indicating that nZVI and the functionalized CNTs were successfully grafted onto the MXene nanosheets. It would also be inferred that nZVI and functionalized CNTs

improved the active sites and some functional groups on MXene, hence improving its performance.

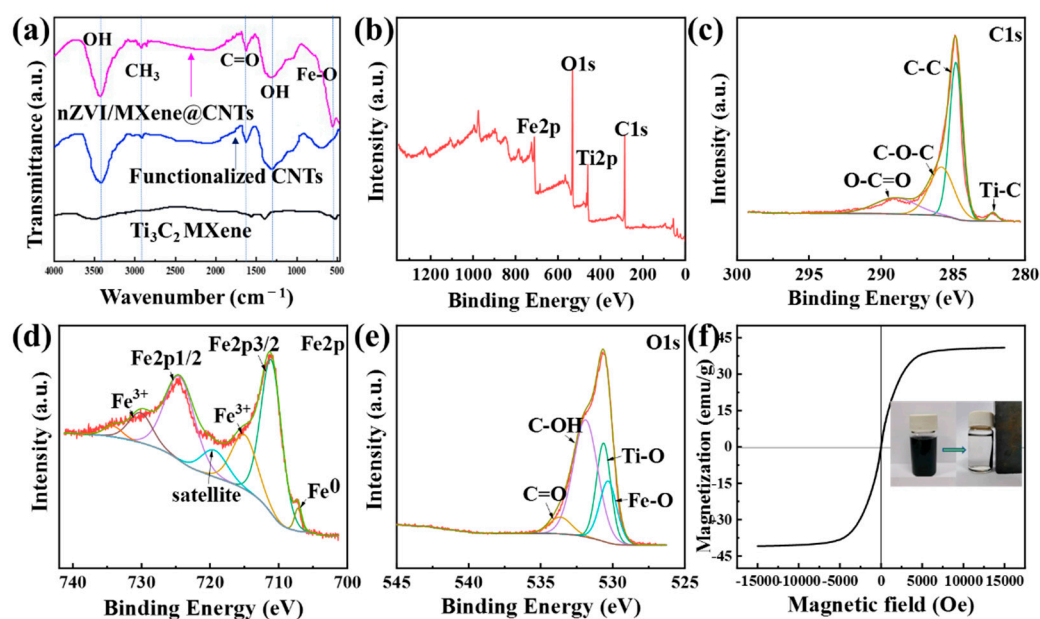


Figure 3. (a) FTIR spectra of Ti_3C_2 MXene, functionalized CNTs and $\text{nZVI}/\text{MXene}@\text{CNTs}$; (b) XPS survey spectra of $\text{nZVI}/\text{MXene}@\text{CNTs}$; (c) C 1s; (d) Fe 2p; (e) O 1s; (f) VSM spectra of $\text{nZVI}/\text{MXene}@\text{CNTs}$.

To better understand the change of the surface functional groups on $\text{nZVI}/\text{MXene}@\text{CNTs}$, the X-ray photoelectron spectroscopy (XPS) analysis was used to discriminate between the types of the functional groups and distinct forms of the elements. As shown in Figure 3b, the peaks in the survey spectrum of $\text{nZVI}/\text{MXene}@\text{CNTs}$ at 285.20, 459.11, 531.24 and 711.52 eV were attributed to C 1s, O 1s and Fe 2p, respectively. The C 1s, Fe 2p and O 1s XPS fine spectra of $\text{nZVI}/\text{MXene}@\text{CNTs}$ are shown in Figure 3c–e. The peaks at 282.15, 284.80, 286.07 and 288.90 eV corresponded to Ti-C, C-C, C-O-C and O-C=O in Figure 3c, respectively [50,51]. The C-C peak was obviously strong, which corresponded to the interactions between the carbon atoms in the carbon nanotubes. In Figure 3d, the peak at 707.16 eV indicated the presence of Fe^0 contained within the nanomaterial. The peaks at 711.07 eV and 724.43 eV suggested that the nZVI nanoparticles on the surfaces were partially oxidized [52,53]. Figure 3e shows that the peaks at 530.23, 530.57, 531.80 and 533.56 eV were attributed to Fe-O, Ti-O, C-OH and C=O, respectively [54], revealing that the functionalized CNTs with abundant oxygen-containing groups successfully loaded onto the materials. Therefore, the XPS results suggested that $\text{nZVI}/\text{MXene}@\text{CNTs}$ were composites composed of Ti_3C_2 , nZVI and CNTs cross-linked together. The hysteresis line diagram of $\text{nZVI}/\text{MXene}@\text{CNTs}$ samples recorded at room temperature with a vibrating sample magnetometer (VSM) is shown in Figure 3f, which shows a ferromagnetic property of 40.93 emu/g. The magnetization strength of the material rapidly fell to zero when the external magnetic field was removed, showing the superparamagnetic [55]. The outstanding magnetic characteristic ensured that the $\text{nZVI}/\text{MXene}@\text{CNTs}$ could be retrieved by an external magnetic field drive after purification of the water body, which significantly helped to overcome the problem of poor recovery and secondary contamination of the nanomaterials in the real treatment of water pollution.

3.2. Removal of As(III) from Aqueous Solutions

3.2.1. Effect of Different Materials

In order to allow for a comparison of the adsorption capacities of different materials, several monomeric and binary materials were chosen to evaluate the As(III) adsorption

performance in this part, and the results are shown in Figure 4a. In comparison to unmodified CNTs, the adsorption of functionalized CNTs were increased by nearly 60%, and the adsorption capacities of nZVI/MXene and MXene/CNTs was increased by about 20.12 mg/g and 141.07 mg/g compared to MXene, respectively. It was indicated that the performance of each component in removing As(III) further improved with the modification of CNTs and the binary and ternary treatment of MXene. It can be inferred that the enhanced performance of nZVI/MXene@CNTs might be related to the introduction of oxygen-containing groups and the increase in a specific surface area, favorably demonstrating its better adsorption performance as a treatment material for the efficient removal of As(III) from water. More interestingly, as shown in Table S1 (Supplementary Materials), the nZVI/MXene@CNTs was much more capable of removing As(III) than the other materials.

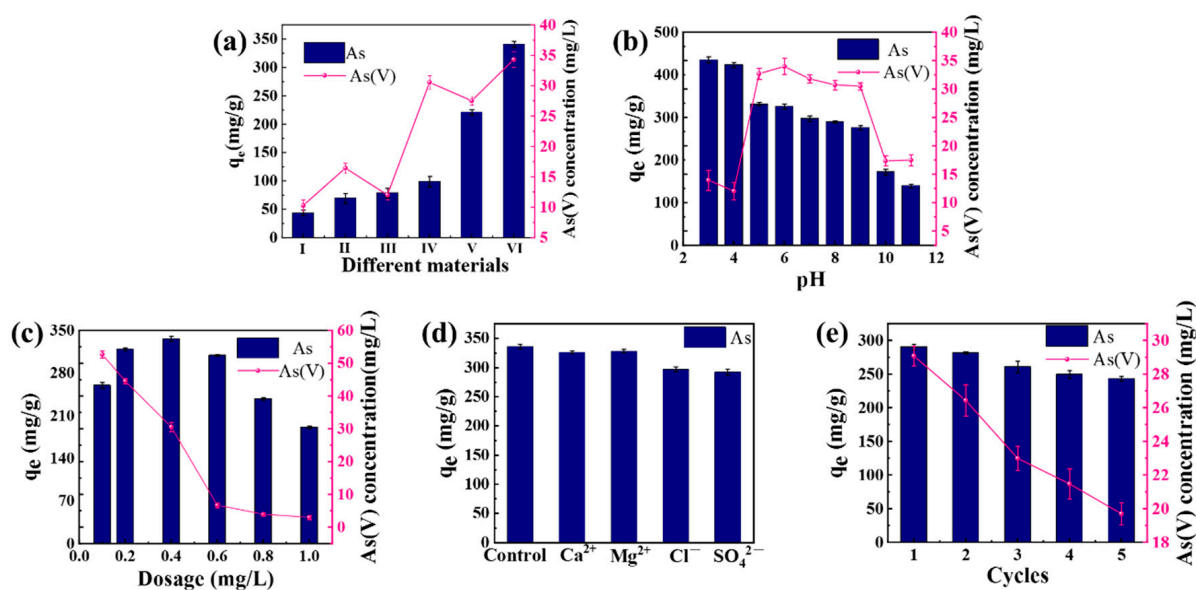


Figure 4. Effect of the (a) different materials, (I–VI representing CNTs, functionalized CNTs, MXene, nZVI/MXene, MXene/CNTs and nZVI/MXene@CNTs, respectively); (b) initial pH; (c) dosage of nZVI/MXene@CNTs; (d) coexisting ionic on the As(III) removal from aqueous solution by nZVI/MXene@CNTs; and (e) reusability of nZVI/MXene@CNTs.

3.2.2. Effect of Initial pH and Dosage

The impact of the initial pH value on As(III) removal by nZVI/MXene@CNTs was studied at room temperature and different pH values in the range 3–11 in an aqueous solution containing 200 mg/L As(III) (Figure 4b). The results clearly showed that the initial pH of the solution had an apparent effect on the remaining concentration and removal rate of As(III). The adsorption capacity of As(III) fell from 443.32 mg/g to 144.95 mg/g when the pH increased from 3.0 to 11.0. The result further demonstrated that the removal of As(III) was limited as the pH levels rose. Under acidic conditions, there were rapid corrosion rates of Fe^0 , accelerating the migration of the electrons in the solution and increasing the reaction rate. Meanwhile, when the pH of the solution was lower than the isoelectric point of the material, the hydroxyl groups on the surface were protonated to produce OH_2^+ to enhance the adsorption of As(V) [56]. At $pH > 9.0$, the removal effect of As(III) decreased significantly, because of the corrosion rate of Fe^0 , and the electron migration rate slowed down, resulting in less H_2O_2 , $\bullet OH$, $\bullet O_2^-$, etc. produced. Meanwhile, As(III) occurred mostly in the form of $H_2AsO_3^-$, and the removal rate decreased due to electrostatic repulsion. Therefore, As(III) was better removed by the nZVI/MXene@CNTs under acidic conditions.

As shown in Figure 4c, the solid-to-liquid ratio of the system would be affected by the dosage. The removal of As(III) by nZVI/MXene@CNTs grew from 12.99% to 97.98% with the increase of the dosage from 0.1 g/L to 1.0 g/L, and the maximum value of adsorption at 0.4 g/L was 336.33 mg/g. That is because, at the same initial concentration, the effective adsorption sites would be enhanced with the dosage appropriately increased. There was a high concentration of As(V) in solution at the lower dosing levels owing to the restricted adsorption sites and the full oxidation of As(III). In contrast, because the adsorption sites were more sufficient at larger dosage, less As(III) and As(V) remained in the solution.

3.2.3. Evaluation of Anti-Ion Interference Capability and Reusability

In the real environment, other anions and cations were certain to be found in the arsenic-containing effluent. To explore the practical application capability of the nZVI/MXene@CNTs, several common interfering ions in water bodies (Ca^{2+} , Mg^{2+} , Cl^- and SO_4^{2-}) were used in the As(III) removal experiment. As shown in Figure 4d, at the 0.01 mol/L concentration of interfering ions, the effect of the As(III) removal rate was in the order of Mg^{2+} (98.60%) > Ca^{2+} (98.09%) > Cl^- (89.21%) > SO_4^{2-} (87.81%). The reason was that the cation would not compete with the negatively charged H_2AsO_3^- for adsorption sites and had basically no effect on the removal of As(III), while the anion would, and then the removal efficiency was restricted [57]. Generally, the nZVI/MXene@CNTs showed a good practical applicability against interference.

Reusability is usually one of the most significant factors to evaluate the performance of adsorbents. Therefore, in addition to the adsorption performance research, the reusability of the materials after desorption should be assessed. In this experiment, 1 mol/L NaOH was used to regenerate the adsorbed composite material, and then employed for further adsorption tests, as shown in Figure 4e. After five cycles, the removal of As(III) by the elution-regenerated nZVI/MXene@CNTs decreased by about 14.25%, which might be owing to a decline in the activity of the number of functional groups and surface active sites. The results showed that the nZVI/MXene@CNTs had outstanding reusability properties and could be employed in true water-treatment procedures.

3.3. Adsorption Kinetics, Isotherms and Thermodynamics

The kinetics are one of the fundamental elements that define the removal efficiency of materials [58]. The influence of reaction time on As(III) elimination is shown in Figure 5e. At environmental temperatures of 15, 25 and 35 °C, the removal reaction achieved equilibrium after about 120 min, with equilibrium adsorption capacities of 317.48, 336.27 and 342.93 mg/g, respectively. Pseudo-first-order and pseudo-second-order models were used to fit the As(III) removal process of the nZVI/MXene@CNTs, and the parameters are listed in Table S2 (Supplementary Materials). As shown, the correlation coefficients R^2 (0.9880, 0.9942, and 0.9893) of the pseudo-second-order fit were greater than those of the pseudo-first-order kinetics (0.9876, 0.9922, and 0.9828), and the overall fit was similarly better. Thus, the rate-controlling step of the reaction was mainly chemisorption.

Langmuir and Freundlich [59] were applied to clarify the adsorption of As(III) by the nZVI/MXene@CNTs from the water solution. The fitting results of the two models are shown in Figure 5c,d, respectively, and the computed parameters of the Langmuir and Freundlich isotherm models are listed in Table S3 (Supplementary Materials). The Langmuir isothermal model could be better described as the adsorption process of nZVI/MXene@CNTs on As(III), implying that the adsorption of nZVI/MXene@CNTs on As(III) occurred primarily on the uniform monolayer boundary of the material. Once saturation was reached, no further reaction would occur at the adsorption site of the surface layer [60]. At the conditions of pH = 5.0 and 25 °C, the predicted maximum adsorption capacity of nZVI/MXene@CNTs was 336.64 mg/g, which was roughly close to the actual maximum adsorption capacity of 333.56 mg/g.

The fitted Van't Hoff plot is shown in Figure 5e, and the thermodynamic data of As(III) removal from the aqueous solution by nZVI/MXene@CNTs are shown in Table S4 (Supplementary Materials). As the initial As(III) concentrations increased from 25 to 300 mg/L, the enthalpy value (ΔH^0) decreased from 94.31 to 8.47 kJ/mol. The fact that all ΔS^0 were positive and all ΔG^0 were negative indicated that the adsorption of As(III) by nZVI/MXene@CNTs was rational and irreversible. The progressive drop in ΔG^0 from 15 °C to 35 °C showed that increasing the temperature allows for a larger spontaneous tendency of the reaction, and the reaction was more likely to occur at higher temperatures. Therefore, As(III) adsorption by nZVI/MXene@CNTs was a spontaneous and endothermic reaction.

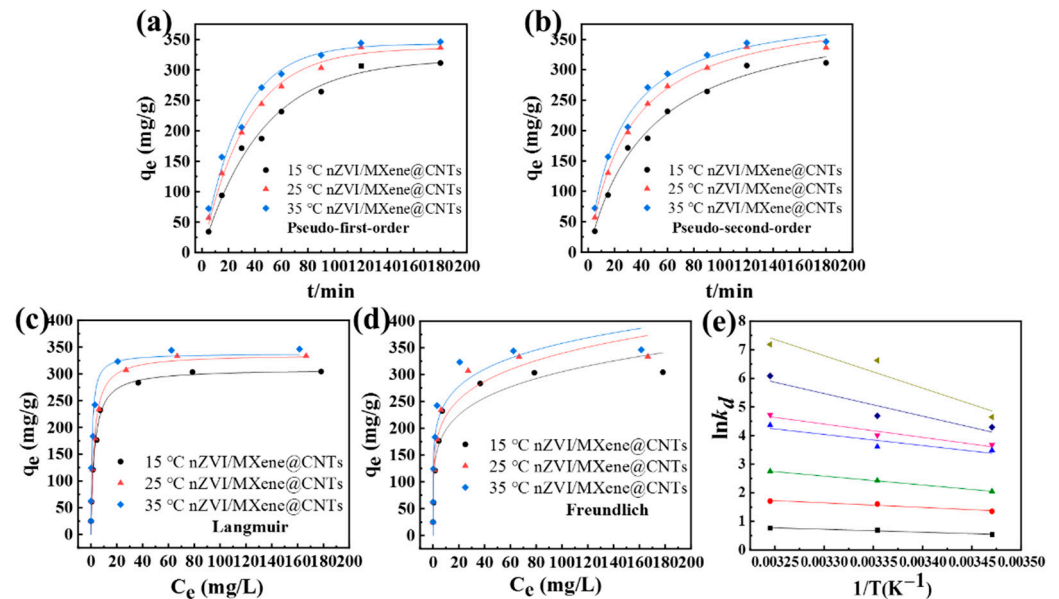


Figure 5. (a) Pseudo-first-order and (b) pseudo-second-order models of nZVI/MXene@CNTs; (c) Langmuir and (d) Freundlich isotherms models of nZVI/MXene@CNTs; (e) thermodynamics of nZVI/MXene@CNTs at different temperatures.

3.4. Mechanism Analysis

To explore the changes in the functional groups, the FTIR analysis was utilized before and after the adsorption of As(III) by nZVI/MXene@CNTs (Figure 6a). The peaks at 3385.74, 1623.91 and 1383.82 cm^{-1} after adsorption corresponded to the -OH stretching, O-C=O symmetric and asymmetric stretching vibrations, respectively [61]. The functional group species were changed slightly before and after the adsorption, while the wave number of absorption peaks were changed, indicating that the aforementioned functional groups might be involved in the removal of As(III). The intensity of the O-C=O peak had increased, which indicated that the ligand process combined As(III) with the carboxylate, possibly producing the free -COOH. The intensity of the -OH peak had dropped, probably due to the Fe-OH breaking, implying that the hydroxyl group was engaged in the reaction and gradually decreased as the reaction progressed. The typical peak of Fe_3O_4 was shifted to 448.47 eV, which might be attributed to the electrostatic gravitational effect between Fe and As(III). The peak at 815.14 eV was corresponded to the Fe-O-As vibrational peak, indicating that As(III) removal process occurred through surface complexation, as well as solid-phase precipitation by bonding As(III) to Fe [62]. The results suggested that the nZVI/MXene@CNTs retained a good magnetic characteristic, making it suitable for recycling [63,64].

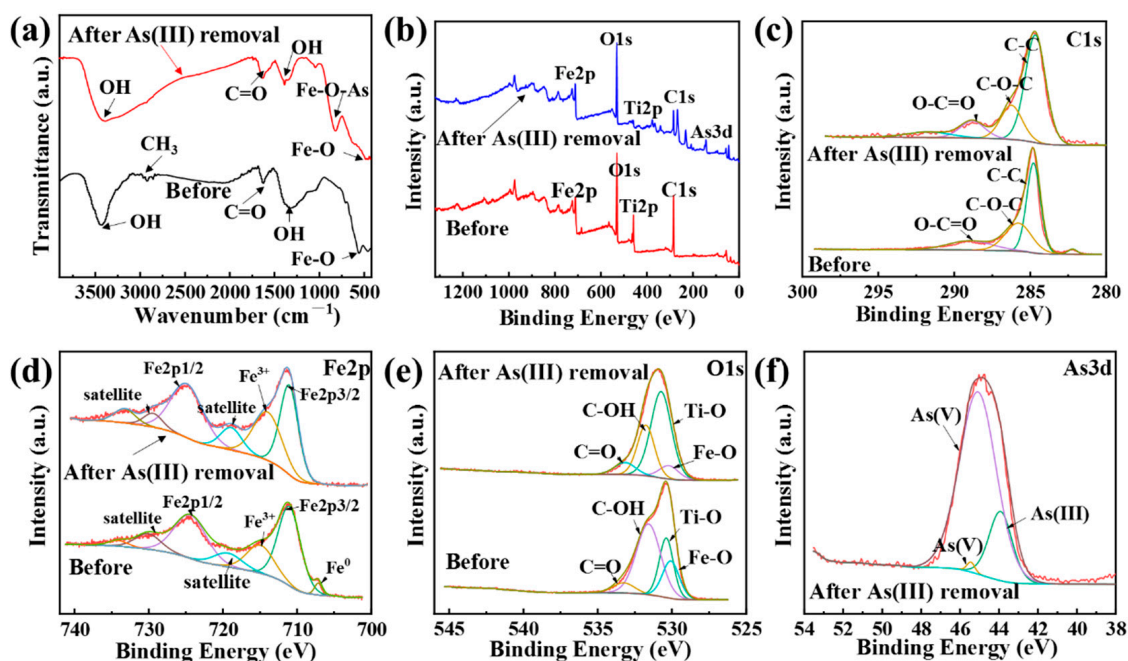


Figure 6. (a) FTIR spectra of nZVI/MXene@CNTs before and after As adsorption; (b) XPS spectra of nZVI/MXene@CNTs before and after As adsorption. High-resolution (c) C 1s; (d) Fe 2p; (e) O 1s XPS spectra of nZVI/MXene@CNTs before and after As adsorption; (f) High-resolution As 3d XPS spectra of nZVI/MXene@CNTs after adsorption.

In order to further investigate the adsorption mechanism of nZVI/MXene@CNTs, the XPS analysis was performed before and after the adsorption of As(III). The obtained XPS full and fine spectrum of each element are shown in Figure 6b–f. There was an additional characteristic peak of As 3d at 44.71 eV, suggesting that As(III) was successfully adsorbed by the nZVI/MXene@CNTs, in addition to the typical peaks of C 1s, Ti 2p, O 1s and Fe 2p at 284.45, 458.37, 530.85 and 711.33 eV, respectively. The characteristic peaks of Fe 2p were unchanged, indicating that the nZVI/MXene@CNTs retained good magnetic properties after adsorption. Furthermore, in Figure 6c, three convex peaks appeared at 284.80, 287.15 and 288.80 eV, corresponding to C-C, C-O-C, and O-C=O, respectively, suggesting that the various groups on the surface remained after adsorption. Thus, the structure was stable and could be utilized repeatedly. As shown in Figure 6d, the binding energy of the associated Fe³⁺ peak decreased from 714.99 to 713.97 eV, implying that the charge density increased while the binding energy decreased, owing to the migration of the outer electrons. Therefore, the Fe³⁺ was involved in the removal process [65]. The change of the Fe⁰ characteristic peak indicated that it was oxidized to form hydrated iron oxide during the removal process. It was clearly observed that the characteristic peaks at 532.78, 531.53, 530.64 and 530.48 eV were attributed to C=O, C-OH, Ti-O and Fe-O, respectively (Figure 6e). However, the C-OH content was reduced after the reaction, which might imply that the hydroxyl groups were consumed during the adsorption process, while the spots were occupied by As(III) and As(V). The results were compatible with the FTIR data. As shown in Figure 6f, the characteristic peak of As 3d appeared in the 42–48 eV interval after the adsorption. The characteristic electron-binding energy of As(III) was lower than that of As(V), as the research reported [66]. As a result, the peak at 44.10 eV might be denoted as As(III), whereas the peaks at 45.19 eV and 45.58 eV might be indicated as As(V), with the atomic percentages of 32.02% and 67.98%, respectively. It was suggested that a significant portion of As(III) was oxidized to As(V) during the adsorption process, due to the nZVI and the abundant oxygen-containing groups.

As shown in Figure 7, the removal process and oxidation mechanism of As(III) from water by nZVI/MXene@CNTs were obtained, based on the aforementioned results

and analyses. In general, the adsorption and catalytic oxidation processes of As(III) by nZVI/MXene@CNTs could be explained in Equations (2)–(5). Specifically, three distinct steps might be identified in the removal of As(III): As(III) was first electrostatically adsorbed to the surface of nZVI/MXene@CNTs; then, it was oxidized to As(V) by the $\bullet\text{OH}$ radical generated by Fe^0 [47]; and finally they were removed by the hydrated iron oxide by interfacial co-precipitation from the aqueous solution.

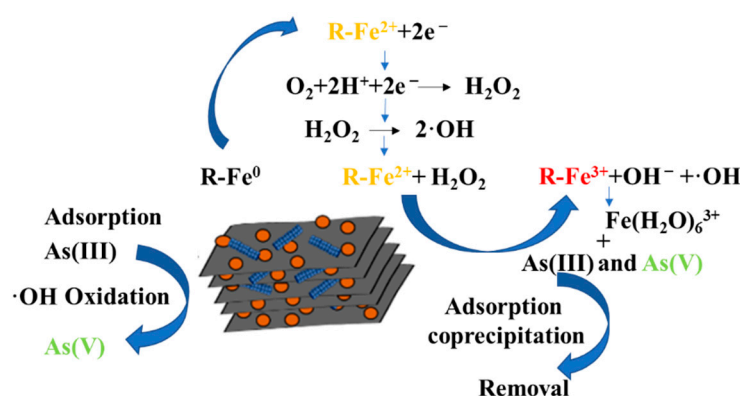
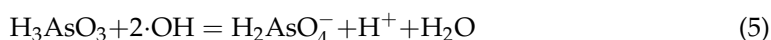


Figure 7. The possible removal mechanism of As(III) by nZVI/MXene@CNTs.

4. Conclusions

In this study, a three-dimensional intercalation $\text{Ti}_3\text{C}_2\text{T}_x$ MXene carbon nanotube supported by nZVI nanocomplex (nZVI/MXene@CNTs) was properly prepared and employed for the rapid adsorption and catalytic oxidation of As(III) in aqueous solution. As a result, the mild method of liquid-phase reduction improved the stability, reactivity and magnetic recovery. The maximum adsorption of nZVI/MXene@CNTs was determined to be 443.32 mg/g in the As(III)-containing solutions with the conditions of pH = 3.0 and 25 °C. The As(III) oxidation process was likely significantly aided by the $\bullet\text{OH}$ that nZVI generated when the nZVI/MXene@CNTs were present, which was obvious under acidic circumstances. The FTIR and XPS analyses and the adsorption model fitting results revealed that the removal of As(III) involved not only surface complexation, but also solid phase precipitation and the oxidation of the $\bullet\text{OH}$. Furthermore, the nZVI/MXene@CNTs could be regenerated by NaOH elution without impacting later usage, demonstrating high reusability. The study provided a cost-effective and ecologically beneficial method for preparing environmentally beneficial and reusable nanomaterials for harmful heavy-metal removal. Therefore, the nZVI/MXene@CNTs had a lot of promise for efficiently purifying toxic metal wastewater and might be employed as an ideal material for water pollution control.

Supplementary Materials: The following supporting information can be downloaded at: <https://www.mdpi.com/article/10.3390/app12168206/s1>, Table S1: Comparison of As(III) removal performance of nZVI/MXene@CNTs and other materials; Table S2: The fitting parameters of pseudo-first-order and pseudo-second-order kinetic models for As(III) adsorption by nZVI/MXene@CNTs; Table S3: The fitting parameters of Langmuir and Freundlich isotherm models for As(III) adsorption by nZVI/MXene@CNTs; Table S4 The fitting parameters of thermodynamic model for As(III) adsorption by nZVI/MXene@CNTs. References [67,68] are cited in the supplementary materials.

Author Contributions: R.C.: Conceptualization, Writing—review and editing; S.L. (Shihai Li): Writing—original draft; S.L. (Siyuan Luo): Investigation, Data curation; S.W.: Methodology, Project administration; P.W.: Supervision; G.Z.: Software; W.W.: Formal analysis, Writing—review and editing. All authors have read and agreed to the published version of the manuscript.

Funding: This research was funded by [the Natural science Foundation of Hunan Province] grant number [2022JJ31014], [Hunan Provincial Key Research Plan Program of China] grant number [2021GK4059 and 2020SK2006] and [the project fund of degree and graduate education reform] grant number [2019JG001]. And the APC was funded by [2022JJ31014 and 2020SK2006].

Institutional Review Board Statement: Not applicable.

Informed Consent Statement: Not applicable.

Data Availability Statement: Data sharing not applicable.

Acknowledgments: This work was supported by the Natural Science Foundation of Hunan Province (2022JJ31014), Hunan Provincial Key Research Plan Program of China (Grant Numbers 2021GK4059 and 2020SK2006) and the project fund of degree and graduate education reform (2019JG001). The authors would like to extend special thanks to the editor and the anonymous reviewers for their constructive comments and suggestions for improving the quality of the paper.

Conflicts of Interest: The authors declare that they have no known competing financial interests or personal relationships that could have appeared to influence the work reported in this paper.

References

1. Yang, L.; Ren, Q.; Zheng, K.; Jiao, Z.; Ruan, X.; Wang, Y. Migration of heavy metals in the soil-grape system and potential health risk assessment. *Sci. Total Environ.* **2022**, *806*, 150646. [[CrossRef](#)] [[PubMed](#)]
2. Chai, L.; Yue, M.; Jinqin, Y.; Qingwei, W.; Qingzhu, L.; Hui, L. Formation of tooeite and the role of direct removal of As (III) from high-arsenic acid wastewater. *J. Hazard. Mater.* **2016**, *320*, 620–627. [[CrossRef](#)] [[PubMed](#)]
3. Chen, Q.; Costa, M. Arsenic: A global environmental challenge. *Annu. Rev. Pharmacol. Toxicol.* **2021**, *61*, 47–63. [[CrossRef](#)]
4. Zou, Y.; Wang, X.; Khan, A.; Wang, P.; Liu, Y.; Alsaedi, A.; Hayat, T.; Wang, X. Environmental remediation and application of nanoscale zero-valent iron and its composites for the removal of heavy metal ions: A review. *Environ. Sci. Technol.* **2016**, *50*, 7290–7304. [[CrossRef](#)] [[PubMed](#)]
5. Wang, L.; Giammar, D. Effects of pH, dissolved oxygen, and aqueous ferrous iron on the adsorption of arsenic to lepidocrocite. *J. Colloid Interface Sci.* **2015**, *448*, 331–338. [[CrossRef](#)]
6. Cheng, Z.; Fu, F.; Dionysiou, D.D.; Tang, B. Adsorption, oxidation, and reduction behavior of arsenic in the removal of aqueous As (III) by mesoporous Fe/Al bimetallic particles. *Water Res.* **2016**, *96*, 22–31. [[CrossRef](#)]
7. Chai, L.; Yue, M.; Li, Q.; Guanshi, Z.; Mengxue, Z.; Qingwei, W.; Hui, L.; Qianwen, L. Enhanced stability of tooeite by hydrothermal method for the fixation of arsenite. *Hydrometallurgy* **2018**, *175*, 93–101. [[CrossRef](#)]
8. Cang, L.; Wang, Y.; Zhou, D.; Yuanhua, D. Heavy metals pollution in poultry and livestock feeds and manures under intensive farming in Jiangsu Province, China. *J. Environ. Sci.* **2004**, *16*, 371–374.
9. Li, Y.; Chen, T. Concentrations of additive arsenic in Beijing pig feeds and the residues in pig manure. *Resour. Conserv. Recycl.* **2005**, *45*, 356–367. [[CrossRef](#)]
10. Hanyong, P.; Bin, H.; Qingqing, L.; Zonglin, Y.; Xiufen, L.; Rongfu, H.; Xing-Fang, L.; J, Z.M.; Chris, L.X. Liquid chromatography combined with atomic and molecular mass spectrometry for speciation of arsenic in chicken liver. *J. Chromatogr. A* **2014**, *1370*, 40–49.
11. D’Angelo, E.; Zeigler, G.; Beck, E.G.; Grove, J.; Sikora, F. Arsenic species in broiler (*Gallus gallus domesticus*) litter, soils, maize (*Zea mays* L.), and groundwater from litter-amended fields. *Sci. Total Environ.* **2012**, *438*, 286–292. [[CrossRef](#)] [[PubMed](#)]
12. Jones, F. A broad view of arsenic. *Poult. Sci.* **2007**, *86*, 2–14. [[CrossRef](#)] [[PubMed](#)]
13. Dong, Y.; Gao, M.; Song, Z.; Qiu, W. As (III) adsorption onto different-sized polystyrene microplastic particles and its mechanism. *Chemosphere* **2020**, *239*, 124792. [[CrossRef](#)]
14. Li, J.; Chen, C.; Zhang, S.; Wang, X. Surface functional groups and defects on carbon nanotubes affect adsorption–desorption hysteresis of metal cations and oxoanions in water. *Environ. Sci. Nano* **2014**, *1*, 488–495. [[CrossRef](#)]
15. Jin, Z.; Wang, X.; Sun, Y.; Ai, Y.; Wang, X. Adsorption of 4-n-nonylphenol and bisphenol-A on magnetic reduced graphene oxides: A combined experimental and theoretical studies. *Environ. Sci. Technol.* **2015**, *49*, 9168–9175. [[CrossRef](#)] [[PubMed](#)]
16. De Gisi, S.; Lofrano, G.; Grassi, M.; Notarnicola, M. Characteristics and adsorption capacities of low-cost sorbents for wastewater treatment: A review. *Sustain. Mater. Technol.* **2016**, *9*, 10–40. [[CrossRef](#)]
17. Kolluru, S.S.; Agarwal, S.; Sireesha, S.; Sreedhar, I.; Kale, S.R. Heavy metal removal from wastewater using nanomaterials-process and engineering aspects. *Process Saf. Environ. Prot.* **2021**, *150*, 323–355. [[CrossRef](#)]

18. Ghorbanzadeh, N.; Jung, W.; Halajnia, A.; Lakzian, A.; Kabra, A.N.; Jeon, B.-H. Removal of arsenate and arsenite from aqueous solution by adsorption on clay minerals. *Geosystem Eng.* **2015**, *18*, 302–311. [[CrossRef](#)]
19. Chammui, Y.; Sooksamiti, P.; Naksata, W.; Thiansem, S.; Arqueropanyo, O.-A. Removal of arsenic from aqueous solution by adsorption on Leonardite. *Chem. Eng. J.* **2014**, *240*, 202–210. [[CrossRef](#)]
20. Niazi, N.K.; Bibi, I.; Shahid, M.; Ok, Y.S.; Shaheen, S.M.; Rinklebe, J.; Wang, H.; Murtaza, B.; Islam, E.; Nawaz, M.F. Arsenic removal by Japanese oak wood biochar in aqueous solutions and well water: Investigating arsenic fate using integrated spectroscopic and microscopic techniques. *Sci. Total Environ.* **2018**, *621*, 1642–1651. [[CrossRef](#)]
21. Nieto-Delgado, C.; Rangel-Mendez, J.R. Anchorage of iron hydro (oxide) nanoparticles onto activated carbon to remove As (V) from water. *Water Res.* **2012**, *46*, 2973–2982. [[CrossRef](#)] [[PubMed](#)]
22. Baby, R.; Saifullah, B.; Hussein, M.Z. Carbon nanomaterials for the treatment of heavy metal-contaminated water and environmental remediation. *Nanoscale Res. Lett.* **2019**, *14*, 341. [[CrossRef](#)] [[PubMed](#)]
23. Lim, J.Y.; Mubarak, N.; Abdullah, E.; Nizamuddin, S.; Khalid, M. Recent trends in the synthesis of graphene and graphene oxide based nanomaterials for removal of heavy metals—A review. *J. Ind. Eng. Chem.* **2018**, *66*, 29–44. [[CrossRef](#)]
24. Baratta, M.; Tursi, A.; Curcio, M.; Cirillo, G.; Nicoletta, F.P.; De Filpo, G. GO-SWCNT Buckypapers as an Enhanced Technology for Water Decontamination from Lead. *Molecules* **2022**, *27*, 4044. [[CrossRef](#)]
25. Baratta, M.; Mastropietro, T.F.; Bruno, R.; Tursi, A.; Negro, C.; Ferrando-Soria, J.s.; Mashin, A.I.; Nezhdanov, A.; Nicoletta, F.P.; De Filpo, G. Multivariate Metal–Organic Framework/Single-Walled Carbon Nanotube Buckypaper for Selective Lead Decontamination. *ACS Appl. Nano Mater.* **2022**, *5*, 5223–5233. [[CrossRef](#)]
26. Ebrahiminezhad, A.; Zare-Hoseinabadi, A.; Sarmah, A.K.; Taghizadeh, S.; Ghasemi, Y.; Berenjian, A. Plant-mediated synthesis and applications of iron nanoparticles. *Mol. Biotechnol.* **2018**, *60*, 154–168. [[CrossRef](#)]
27. Abdallah, M.A.M. Removing two transition metal ions from spiked wastewater by two modified nano-sorbents. *Cogent Eng.* **2022**, *9*, 2035133. [[CrossRef](#)]
28. Kong, C.; Liu, F.; Sun, H.; Zhang, Z.; Zhu, B.; Li, W. Co₃O₄/GO catalyst as efficient heterogeneous catalyst for degradation of wastewater containing polyacrylamide (PAM). *Water Cycle* **2021**, *2*, 15–22. [[CrossRef](#)]
29. Sohal, N.; Maity, B.; Shetti, N.P.; Basu, S. Biosensors based on MnO₂ nanostructures: A review. *ACS Appl. Nano Mater.* **2021**, *4*, 2285–2302. [[CrossRef](#)]
30. Kanel, S.R.; Manning, B.; Charlet, L.; Choi, H. Removal of arsenic (III) from groundwater by nanoscale zero-valent iron. *Environ. Sci. Technol.* **2005**, *39*, 1291–1298. [[CrossRef](#)]
31. Zhang, S.; Niu, H.; Cai, Y.; Zhao, X.; Shi, Y. Arsenite and arsenate adsorption on coprecipitated bimetal oxide magnetic nanomaterials: MnFe₂O₄ and CoFe₂O₄. *Chem. Eng. J.* **2010**, *158*, 599–607. [[CrossRef](#)]
32. Wei, Y.; Liu, C.; Luo, S.; Ma, J.; Zhang, Y.; Feng, H.; Yin, K.; He, Q. Deep oxidation and removal of arsenite in groundwater by rationally positioning oxidation and adsorption sites in binary Fe–Cu oxide/TiO₂. *Chem. Eng. J.* **2018**, *354*, 825–834. [[CrossRef](#)]
33. Zhang, H.; Gu, L.; Zhang, L.; Zheng, S.; Wan, H.; Sun, J.; Zhu, D.; Xu, Z. Removal of aqueous Pb (II) by adsorption on Al₂O₃-pillared layered MnO₂. *Appl. Surf. Sci.* **2017**, *406*, 330–338. [[CrossRef](#)]
34. Kanel, S.R.; Greneche, J.-M.; Choi, H. Arsenic (V) removal from groundwater using nano scale zero-valent iron as a colloidal reactive barrier material. *Environ. Sci. Technol.* **2006**, *40*, 2045–2050. [[CrossRef](#)] [[PubMed](#)]
35. Huang, P.; Ye, Z.; Xie, W.; Chen, Q.; Li, J.; Xu, Z.; Yao, M. Rapid magnetic removal of aqueous heavy metals and their relevant mechanisms using nanoscale zero valent iron (nZVI) particles. *Water Res.* **2013**, *47*, 4050–4058. [[CrossRef](#)] [[PubMed](#)]
36. Yan, W.; Herzog, A.A.; Kiely, C.J.; Zhang, W.-x. Nanoscale zero-valent iron (nZVI): Aspects of the core-shell structure and reactions with inorganic species in water. *J. Contam. Hydrol.* **2010**, *118*, 96–104. [[CrossRef](#)]
37. Li, Q.; Zhang, M.; Yang, J.; Liu, Q.; Zhang, G.; Liao, Q.; Liu, H.; Wang, Q. Formation and stability of biogenic tooeleite during Fe (II) oxidation by Acidithiobacillus ferrooxidans. *Mater. Sci. Eng. C* **2020**, *111*, 110755. [[CrossRef](#)]
38. Grieger, K.D.; Fjordbøge, A.; Hartmann, N.B.; Eriksson, E.; Bjerg, P.L.; Baun, A. Environmental benefits and risks of zero-valent iron nanoparticles (nZVI) for in situ remediation: Risk mitigation or trade-off? *J. Contam. Hydrol.* **2010**, *118*, 165–183. [[CrossRef](#)]
39. Shulpekova, A.; Lepakova, O.; Kitler, V.; Golobokov, N.; Afanas'ev, N. Ti–Al–C MAX Phases and Ti–C MXenes via SHS Route and Acid Leaching. *Int. J. Self-Propagating High-Temp. Synth.* **2021**, *30*, 159–164. [[CrossRef](#)]
40. Velusamy, K.; Chellam, P.; Kumar, P.S.; Venkatachalam, J.; Periyasamy, S.; Saravanan, R. Functionalization of MXene-based nanomaterials for the treatment of micropollutants in aquatic system: A review. *Environ. Pollut.* **2022**, *301*, 119034. [[CrossRef](#)]
41. Kim, S.; Gholamirad, F.; Yu, M.; Park, C.M.; Jang, A.; Jang, M.; Taheri-Qazvini, N.; Yoon, Y. Enhanced adsorption performance for selected pharmaceutical compounds by sonicated Ti₃C₂T_x MXene. *Chem. Eng. J.* **2021**, *406*, 126789. [[CrossRef](#)]
42. Jun, B.; Jang, M.; Park, C.M.; Han, J.; Yoon, Y. Selective adsorption of Cs⁺ by MXene (Ti₃C₂T_x) from model low-level radioactive wastewater. *Nucl. Eng. Technol.* **2020**, *52*, 1201–1207. [[CrossRef](#)]
43. Kumar, J.A.; Prakash, P.; Krithiga, T.; Amarnath, D.J.; Premkumar, J.; Rajamohan, N.; Vasseghian, Y.; Saravanan, P.; Rajasimman, M. Methods of synthesis, characteristics, and environmental applications of MXene: A comprehensive review. *Chemosphere* **2022**, *286*, 131607. [[CrossRef](#)] [[PubMed](#)]
44. Xiao, Z.; Li, Z.; Meng, X.; Wang, R. MXene-engineered lithium–sulfur batteries. *J. Mater. Chem. A* **2019**, *7*, 22730–22743. [[CrossRef](#)]
45. You, Z.; Liao, Y.; Li, X.; Fan, J.; Xiang, Q. State-of-the-art recent progress in MXene-based photocatalysts: A comprehensive review. *Nanoscale* **2021**, *13*, 9463–9504. [[CrossRef](#)]

46. Jiang, Q.; Lei, Y.; Liang, H.; Xi, K.; Xia, C.; Alshareef, H.N. Review of MXene electrochemical microsupercapacitors. *Energy Storage Mater.* **2020**, *27*, 78–95. [[CrossRef](#)]
47. Chen, R.; Cheng, Y.; Ping, W.; Wang, Y.; Wang, Q.; Yang, Z.; Tang, C.; Xiang, S.; Luo, S.; Huang, S.; et al. Facile synthesis of a sandwiched $\text{Ti}_3\text{C}_2\text{T}_x$ MXene/nZVI/fungal hypha nanofiber hybrid membrane for enhanced removal of Be(II) from Be(NH)₂ complexing solutions. *Chem. Eng. J.* **2021**, *421*, 129682. [[CrossRef](#)]
48. Wang, Y.; Zheng, K.; Zhan, W.; Huang, L.; Liu, Y.; Li, T.; Yang, Z.; Liao, Q.; Chen, R.; Zhang, C.J.E.; et al. Highly effective stabilization of Cd and Cu in two different soils and improvement of soil properties by multiple-modified biochar. *Ecotoxicol. Environ. Saf.* **2021**, *207*, 111294. [[CrossRef](#)]
49. Han, L.; Li, B.; Tao, S.; An, J.; Fu, B.; Han, Y.; Li, W.; Li, X.; Peng, S.; Yin, T. Graphene oxide-induced formation of a boron-doped iron oxide shell on the surface of NZVI for enhancing nitrate removal. *Chemosphere* **2020**, *252*, 126496. [[CrossRef](#)]
50. Liu, C.; Zhang, H.; Li, R.; Li, X.; Tang, P.; Wang, Y.; Yang, B.; Qiao, Z.; Yang, G. Laser triggered exothermic chemical reaction in Au nanoparticle@ Ti_3C_2 MXene membrane: A route toward efficient light to high-temperature pulse conversion. *Chem. Eng. J.* **2021**, *420*, 127672. [[CrossRef](#)]
51. Zana, A.; Rüdiger, C.; Kunze-Liebhäuser, J.; Granozzi, G.; Reeler, N.E.; Vosch, T.; Kirkensgaard, J.J.; Arenz, M. Core-shell TiO_2 @C: Towards alternative supports as replacement for high surface area carbon for PEMFC catalysts. *Electrochim. Acta* **2014**, *139*, 21–28. [[CrossRef](#)]
52. Lei, J.; Liu, H.; Yin, D.; Zhou, L.; Liu, J.A.; Chen, Q.; Cui, X.; He, R.; Duan, T.; Zhu, W. Boosting the loading of metal single atoms via a bioconcentration strategy. *Small* **2020**, *16*, 1905920. [[CrossRef](#)] [[PubMed](#)]
53. Zhu, F.; Wu, Y.; Liang, Y.; Li, H.; Liang, W. Degradation mechanism of norfloxacin in water using persulfate activated by BC@nZVI/Ni. *Chem. Eng. J.* **2020**, *389*, 124276. [[CrossRef](#)]
54. Zheng, C.; Yisen, Z.; Ma, J.; Liu, C.; Ma, Y. Detailed XPS analysis and anomalous variation of chemical state for Mn- and V-doped TiO_2 coated on magnetic particles. *Ceram. Int.* **2017**, *43*, 16763–16772.
55. Ling, L.; Pan, B.; Zhang, W.-x. Removal of selenium from water with nanoscale zero-valent iron: Mechanisms of intraparticle reduction of Se (IV). *Water Res.* **2015**, *71*, 274–281. [[CrossRef](#)]
56. Yang, X.; Shi, M.; Leng, D.; Zhang, W.-b. Fabrication of a porous hydrangea-like Fe_3O_4 @ MnO_2 composite for ultra-trace arsenic preconcentration and determination. *Talanta* **2018**, *189*, 55–64. [[CrossRef](#)]
57. Pan, G.; Chong, S.; Pan, K.-L.; Chang, M.-B.; Yang, T.C.-K.; Shukla, P. The study of photoelectrochemical properties of LaMnO_3 , LaFeO_3 , LaCrO_3 , and LaNiO_3 photoelectrodes for hydrogen production. *Clean Technol. Environ. Policy* **2017**, *19*, 1557–1565. [[CrossRef](#)]
58. Zhang, X.; Yan, L.; Li, J.; Yu, H. Adsorption of heavy metals by l-cysteine intercalated layered double hydroxide: Kinetic, isothermal and mechanistic studies. *J. Colloid Interface Sci.* **2020**, *562*, 149–158. [[CrossRef](#)]
59. Mahmoud, M.E.; Nabil, G.M.; Abdel-Aal, H.; Fekry, N.A.; Osman, M.M. Imprinting “Nano- SiO_2 -crosslinked chitosan-Nano- TiO_2 ” polymeric nanocomposite for selective and instantaneous microwave-assisted sorption of Hg (II) and Cu (II). *ACS Sustain. Chem. Eng.* **2018**, *6*, 4564–4573. [[CrossRef](#)]
60. Tuutijärvi, T.; Lu, J.; Sillanpää, M.; Chen, G. As (V) adsorption on maghemite nanoparticles. *J. Hazard. Mater.* **2009**, *166*, 1415–1420. [[CrossRef](#)]
61. Hui, Z.; Qiang, R.; Zheng, K.; Qin, Z.; Wang, Y.; Wang, Y. Spatial distribution and risk assessment of metal (loid) s in marine sediments in the Arctic Ocean and Bering Sea. *Mar. Pollut. Bull.* **2022**, *179*, 113729.
62. Yang, L.; Ren, Q.; Ge, S.; Jiao, Z.; Zhan, W.; Hou, R.; Ruan, X.; Pan, Y.; Wang, Y. Metal (loid) s Spatial Distribution, Accumulation, and Potential Health Risk Assessment in Soil-Wheat Systems near a Pb/Zn Smelter in Henan Province, Central China. *Int. J. Environ. Res. Public Health* **2022**, *19*, 2527. [[CrossRef](#)] [[PubMed](#)]
63. Li, Q.; Liu, Q.; Wang, X.; Liao, Q.; Liu, H.; Wang, Q. Yeast extract affecting the transformation of biogenic tooleite and its stability. *Appl. Sci.* **2022**, *12*, 3290. [[CrossRef](#)]
64. Shi, Q.; Zhang, Y.; Sun, D.; Zhang, S.; Tang, T.; Zhang, X.; Cao, S. Bi_2O_3 -sensitized TiO_2 hollow photocatalyst drives the efficient removal of tetracyclines under visible light. *Inorg. Chem.* **2020**, *59*, 18131–18140. [[CrossRef](#)]
65. Ahmad, S.; Liu, X.; Tang, J.; Zhang, S. Biochar-supported nanosized zero-valent iron (nZVI/BC) composites for removal of nitro and chlorinated contaminants. *Chem. Eng. J.* **2022**, *431*, 133187. [[CrossRef](#)]
66. Adio, S.O.; Omar, M.H.; Asif, M.; Saleh, T.A. Arsenic and selenium removal from water using biosynthesized nanoscale zero-valent iron: A factorial design analysis. *Process Saf. Environ. Prot.* **2017**, *107*, 518–527. [[CrossRef](#)]
67. Ye, X.; Ren, G. Adsorption of As(III) from aqueous solution by amidated/oxidized carbon nanotube-polyaniline. *Chin. J. Environ. Eng.* **2019**, *13*, 2798–2807.
68. Sherlala, A.I.A.; Raman, A.A.A.; Bello, M.M.; Buthiyappan, A. Adsorption of arsenic using chitosan magnetic graphene oxide nanocomposite. *J. Environ. Manag.* **2019**, *246*, 547–556. [[CrossRef](#)]